



The Connection Between Galactic Outflows and the Escape of Ionizing Photons

Ramesh Mainali^{1,2}, Jane R. Rigby¹, John Chisholm³, Matthew Bayliss⁴, Rongmon Bordoloi⁵, Michael D. Gladders⁶, T. Emil Rivera-Thorsen⁷, Håkon Dahle⁸, Keren Sharon⁹, Michael Florian¹⁰, Danielle A. Berg³, Soniya Sharma¹, M. Riley Owens⁴, Karin Kjellgren⁷, Keunho J. Kim⁴, and Julia Wayne⁴

¹ Observational Cosmology Lab, Code 665, NASA Goddard Space Flight Center, Greenbelt, MD 20771, USA; ramesh.mainali@nasa.gov, jane.r.rigby@nasa.gov

² Department of Physics, The Catholic University of America, Washington, DC 20064, USA

³ Astronomy Department, University of Texas at Austin, 2515 Speedway, Stop C1400, Austin, TX 78712-1205, USA

⁴ Department of Physics, University of Cincinnati, Cincinnati, OH 45221, USA

⁵ Department of Physics, North Carolina State University, Raleigh, NC 27695, USA

⁶ Department of Astronomy & Astrophysics, The University of Chicago, 5640 S. Ellis Avenue, Chicago, IL 60637, USA

⁷ The Oskar Klein Centre, Department of Astronomy, Stockholm University, AlbaNova, SE-10691 Stockholm, Sweden

⁸ Institute of Theoretical Astrophysics, University of Oslo, P.O. Box 1029, Blindern, NO-0315 Oslo, Norway

⁹ University of Michigan, Department of Astronomy, 1085 South University Avenue, Ann Arbor, MI 48109, USA

¹⁰ Steward Observatory, University of Arizona, 933 North Cherry Ave., Tucson, AZ 85721, USA

Received 2022 August 7; revised 2022 October 17; accepted 2022 October 20; published 2022 December 1

Abstract

We analyze spectra of a gravitationally lensed galaxy, known as the Sunburst Arc, that is leaking ionizing photons, also known as the Lyman continuum (LyC). Magnification from gravitational lensing permits the galaxy to be spatially resolved into one region that leaks ionizing photons and several that do not. Rest-frame UV and optical spectra from Magellan target 10 different regions along the lensed Arc, including six multiple images of the LyC leaking region and four regions that do not show LyC emission. The rest-frame optical spectra of the ionizing photon emitting regions reveal a blueshifted ($\Delta V = 27 \text{ km s}^{-1}$) broad emission component (FWHM = 327 km s^{-1}), comprising 55% of the total [O III] line flux, in addition to a narrow component (FWHM = 112 km s^{-1}), suggesting the presence of strong highly ionized gas outflows. This is consistent with the high-velocity ionized outflow inferred from the rest-frame UV spectra. In contrast, the broad emission component is less prominent in the nonleaking regions, comprising $\sim 26\%$ of total [O III] line flux. The high-ionization absorption lines are prominent in both the leaker and the nonleaker, but the low-ionization absorption lines are very weak in the leaker, suggesting that the line-of-sight gas is highly ionized in the leaker. Analyses of stellar wind features reveal that the stellar population of the LyC leaking regions is considerably younger ($\sim 3 \text{ Myr}$) than that of the nonleaking regions ($\sim 12 \text{ Myr}$), emphasizing that stellar feedback from young stars may play an important role in ionizing photon escape.

Unified Astronomy Thesaurus concepts: [High-redshift galaxies \(734\)](#); [Reionization \(1383\)](#)

1. Introduction

Understanding the epoch of reionization (EoR), when the last phase transition of the universe occurred, is one of the longstanding goals of extragalactic astronomy. The massive stars residing in these high-redshift star-forming galaxies are suspected to be the dominant ionizing agents that drive reionization (e.g., Finkelstein et al. 2019; Robertson et al. 2015), although some studies suggest that low-luminosity active galactic nuclei (AGNs) may play a significant role in reionization (e.g., Madau & Haardt 2015; Kulkarni et al. 2019). The study of reionization requires understanding the rate at which ionizing photons are injected into the intergalactic medium (IGM) by the galaxy population, known as ionizing emissivity (e.g., Robertson et al. 2015; Finkelstein et al. 2019). In practice, this quantity can be measured by combining three key factors: the rest-frame UV luminosity density (ρ_{UV}), the ionizing photon production efficiency (ξ_{ion}), and the fraction of ionizing photons that escapes from galaxies (f_{esc}). Soon, the James Webb Space Telescope (JWST) will measure the first two quantities at the EoR, but the measurement of f_{esc} will rely heavily on indirect probes at high redshift or work on analogs

at lower redshift, since ionizing fluxes cannot be measured at $z > 6$, due to the large opacity of the IGM. Further progress hinges on understanding the detailed astrophysics of how ionizing photons escape from Lyman continuum (LyC) emitting systems at lower redshift.

Galaxy-scale outflows are one of the main suspects in aiding the escape of ionizing photons from galaxies (e.g., Weiner et al. 2009; Heckman et al. 2011; Newman et al. 2012; Jones et al. 2013; Bordoloi et al. 2014; Rubin et al. 2014; Alexandroff et al. 2015; Chisholm et al. 2017; Kim et al. 2020). These outflows are expected to remove the surrounding neutral gas, thus clearing a pathway for the ionizing photons to escape efficiently. However, it is often challenging to reconcile the timescales of such strong galactic outflows with the timescales of the production and escape of ionizing photons in a galaxy. This has been demonstrated in cosmological simulations, where detailed treatments of the multiphase interstellar medium (ISM) and feedback were possible, yet very low f_{esc} , at the level of only a few percent, were predicted (e.g., Gnedin et al. 2008; Kim et al. 2013; Wise et al. 2014; Ma et al. 2015; Rosdahl et al. 2018). In these simulations, most of the ionizing photons are consumed by surrounding neutral gas clouds (e.g., Ma et al. 2015; Kimm et al. 2017; Kakiichi & Gronke 2021). The feedback from supernova (SN) activity may help with the ionizing photon escape, but SNe first occur after about 3 Myr of massive star formation, and peak at around

10 Myr. On the other hand, the ionizing photon production from massive stars begins to decline after 3 Myr, thus allowing for a very narrow timing window for the escape of the ionizing photons (Ma et al. 2015).

Recent progress on the above picture has come from high-resolution cosmological simulations of LyC emitting sources in the EoR (Ma et al. 2020), studying $z > 5$ simulated galaxies from the Feedback in Realistic Environments project (Hopkins et al. 2018). The most recent version of the simulations incorporates the multiphase ISM, star formation, and stellar feedback. The study finds that the majority of the LyC escape comes from the very young (< 10 Myr), vigorously star-forming regions of a galaxy, with negligible contribution from an older (> 10 Myr) stellar population. The LyC escaping sites are often characterized by feedback-driven kiloparsec-scale superbubbles, which clear out the neutral gas column to allow the escape of the ionizing photons.

In order to test the theoretical picture discussed above, we must study LyC emitting galaxies in detail to determine the astrophysics that regulate the escape of LyC photons into the IGM. Galaxies at redshifts above ~ 0.1 are in general too distant to study in any detail. Rest-UV spectra of nearby galaxies require observations with the Cosmic Origins Spectrograph on the Hubble Space Telescope (HST), whose $2''.5$ aperture makes it impossible to pinpoint LyC sources on scales smaller than hundreds of parsecs for the closest galaxies. However, lower-redshift LyC emitters are very rare; only three have been discovered at $z < 0.1$ (Leitet et al. 2011, 2013; Leitherer et al. 2016). The average measured LyC escape fractions are found to be only a few percent, suggesting that very little ionizing radiation of stellar origin escapes from galaxies. At slightly higher redshifts, $z \sim 0.1\text{--}0.4$, ‘‘Green Pea’’ galaxies are found to be LyC emitters, with escape fractions up to $\sim 75\%$ (Borthakur et al. 2014; Izotov et al. 2016, 2018, 2021; Flury et al. 2022a). Recently, several programs have discovered LyC emitting galaxies at $1.5 \lesssim z \lesssim 4$; only a handful of these galaxies show large LyC escape fractions (Shapley et al. 2016; Vanzella et al. 2016, 2018; Bian et al. 2017; Steidel et al. 2018; Fletcher et al. 2019; Rivera-Thorsen et al. 2019). Overall, the results from lower-redshift LyC studies suggest that the LyC escape from an average galaxy population that is significantly lower than that required to drive cosmic reionization. It is thus crucial to understand the key differences between lower-redshift and EoR galaxies, and how they impact the overall escape of LyC photons.

Highly magnified lensed galaxies at $z > 1$ with significant LyC leakage may present the most tractable sites for studying the escape of ionizing photons at any redshift. This point is powerfully demonstrated by the Sunburst Arc at $z = 2.37$ (Dahle et al. 2016; Rivera-Thorsen et al. 2017, 2019; Chisholm et al. 2019), also known as PSZ1-ARC G311.660218.4624, one of the brightest gravitationally lensed galaxies known. HST observations in the rest-frame LyC (the observed F275W band) clearly show that this galaxy appears 12 times in the image plane, with a significant amount of leakage of ionizing photons (Rivera-Thorsen et al. 2019). The LyC emitting region has a highly unusual triple-peaked Ly α line profile, which Rivera-Thorsen et al. (2017) interpret as evidence that the radiation escapes through a narrow empty channel in an otherwise optically thick medium.

This paper leverages rest-frame UV and optical spectroscopy of multiple distinct regions within the Sunburst Arc to compare

regions that leak LyC photons to those that do not. This allows us to connect the properties of the outflows to their local driving sources. Rest-frame UV spectra from the Magellan Echellette (MagE; Marshall et al. 2008) instrument on the Magellan/Baade telescope constrain the massive stellar population, as well as the ISM. Rest-frame optical spectra from the Folded-port InfraRed Echelle (FIRE; Simcoe et al. 2008) instrument on Magellan/Baade constrain the nebular gas.

The paper is organized as follows. We discuss our observational strategy and the data reduction in Section 2. In Section 3, we discuss the methodology, before we present our analysis in Section 4. We discuss the implications for the physical picture of ionizing photon escape and the inferred size scale of the outflowing gas in Section 5, and we summarize our findings in Section 6. Throughout this paper, we adopt a Λ -dominated flat universe, with $\Omega_\Lambda = 0.7$, $\Omega_M = 0.3$, and $H_0 = 70 \text{ h}_{70} \text{ km s}^{-1} \text{ Mpc}^{-1}$. All magnitudes are quoted in the AB system. Equivalent widths (EWs) are quoted in rest frame, unless stated otherwise.

2. Observations

2.1. Magellan/FIRE Near-IR Spectroscopy

We observed the Sunburst Arc over the course of three observing runs from 2016 to 2018. We used the FIRE (Simcoe et al. 2008) instrument on Magellan in echelle mode, providing continuous spectral coverage for wavelengths between 0.82 and $2.51 \mu\text{m}$. We adopted a slit width of $0''.6$, resulting in a resolving power of $R = 6000$. 10 different regions within the arc are observed, including both LyC emitting and nonemitting regions. The orientations of the 10 different slits are shown in Figure 1. The exposures were carried out using two dither positions separated by $3''.0$. We obtained a total exposure of 9.08 hr, with an average exposure of 54.5 minutes per slit position. The slits were positioned on the sky by directly acquiring one of two nearby reference stars (see Figure 1), then applying small ($\lesssim 1''$) coordinated offsets to move the slit onto the desired location along the arc.

The FIRE spectra were reduced using the standard routines in the FIREHOSE data reduction pipeline.¹¹ The pipeline calculates 2D sky models iteratively, following Kelson (2003). The wavelength solutions are provided by fitting OH skylines in the science spectra. Flux calibration and telluric corrections are applied using A0V star observations that were obtained immediately before or after the science observations. The 1D spectra were extracted by using optimal extraction, obtained by calculating the spatial profiles of the strongest well-isolated emission lines in the FIRE spectra (i.e., [O III] λ 5007).

2.2. Near-IR HST Grism Spectroscopy

The near-IR spectra of the Sunburst Arc were obtained using the HST WFC3/IR G141 grism, from program GO-15101 (PI: H. Dahle). The WFC3/IR G141 grism covers wavelengths from 1.075 to $1.7 \mu\text{m}$ and has a resolving power of $R \sim 130$. At the redshift of the Sunburst Arc ($z = 2.37$), the G141 grism covers a rest-frame wavelength of ~ 3200 to 5040 \AA , allowing measurements of all emission lines from [O II] λ 3727 to [O III] λ 5007. The grism observations were performed at two different orientation angles ($27^\circ.37$ and $355^\circ.37$), as is standard

¹¹ wikis.mit.edu/confluence/display/FIRE/FIRE+Data+Reduction

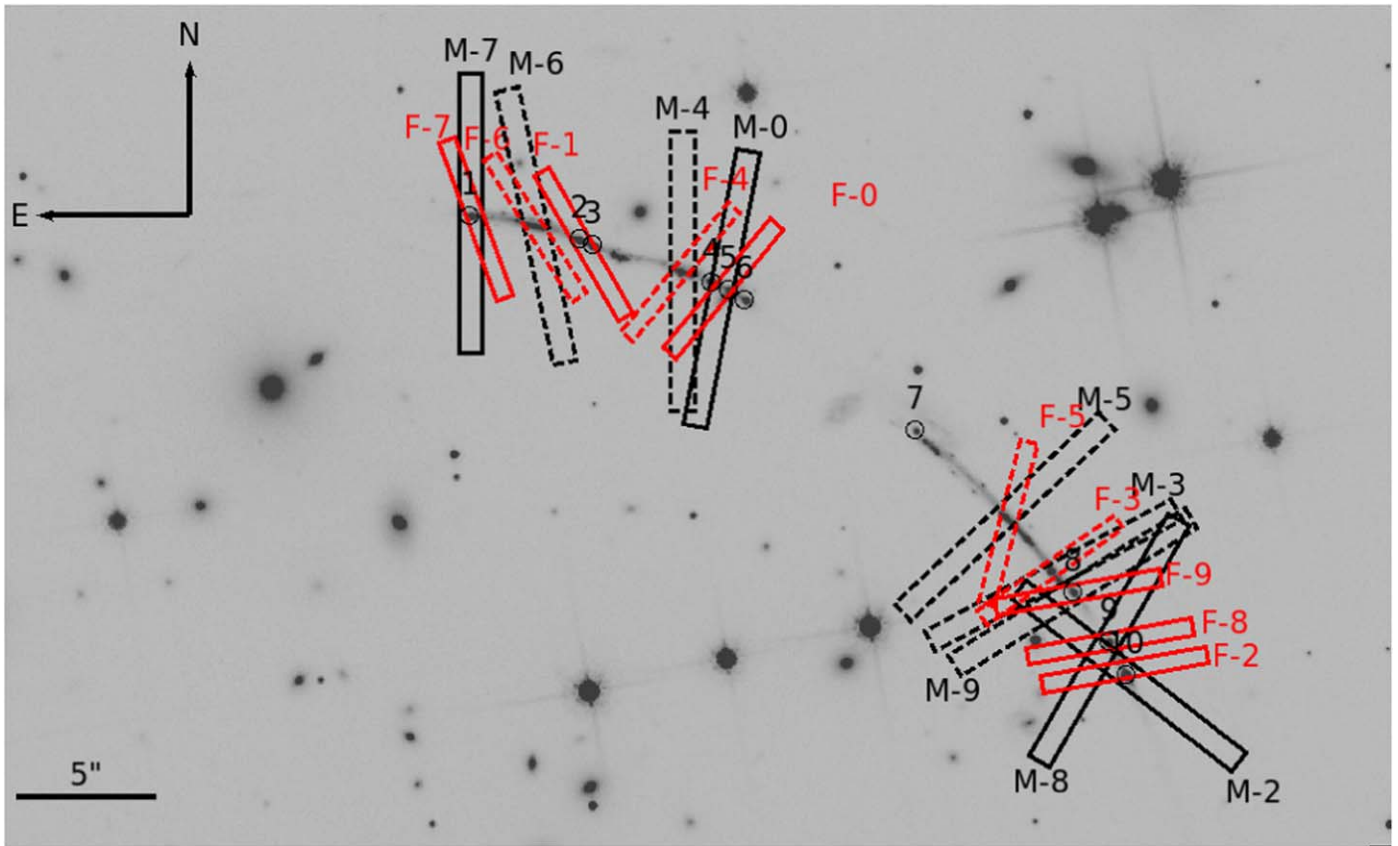


Figure 1. HST F814W image of the Sunburst Arc, showing the positions of the FIRE and MagE slits. The red rectangles show the positions and orientations of 10 FIRE slits, and the black rectangles show the positions and orientations of nine MagE slits. The solid and dashed rectangles indicate knots leaking and not leaking LyC photons, respectively. The numbers indicate multiple images of a LyC emitting region.

practice for mitigating contamination from cluster galaxies. The total grism integration time was 8.42 Ks.

The HST grism spectra were reduced following the procedures described in Florian et al. (2021). To summarize, we used the software package Grizli13 (Brammer 2018), following the standard steps, plus an extra step of GALFIT modeling (Peng et al. 2010) of the contamination from more than 80 foreground stars and cluster galaxies. Since the galactic coordinates of the Sunburst Arc are close to the Galactic plane, there are more foreground stars in the field of view than is typical for lensed galaxies. Most of the grism spectra are thus contaminated by foreground star lights at several locations. In this paper, we focus on the grism spectrum of LyC emitting knot 3, which is devoid of any contaminant, allowing reliable measurements of both continuum and emission lines. The continuum and emission lines in the spectra were fit as described in Rigby et al. (2021).

2.3. Magellan/MagE Optical Spectroscopy

Observations of the Sunburst Arc with the MagE spectrograph (Marshall et al. 2008) were made as part of the extension to the Magellan Evolution of Galaxies Spectroscopic and Ultraviolet Reference Atlas (MEGAsaURA). The main MEGAsaURA survey is described in Rigby et al. (2018); the MEGAsaURA extension will be described in J. Rigby et al. (in preparation). Here, we summarize the key observational details. The observations were conducted with MagE, mounted on the Magellan/Baade telescope. Target acquisition was performed by offsetting from a nearby bright star, with the acquisition

being verified from the slit-viewing guide camera. Nine slit positions were obtained; all used the $0''.85$ slit width, except slit position M-0, which used the $1''$ slit width—motivated by the atmospheric seeing during the observing runs. These observations overlap with nine of the 10 FIRE slit positions. This overlap enables joint analysis of the rest-frame UV and optical spectra. The MagE slit positions corresponding to the FIRE positions are given in Table 1.

The MagE spectra cover observed wavelengths of 3200–8280 Å. For the Sunburst Arc at $z = 2.37$, this results in rest-frame wavelength coverage of 950 Å to 2457 Å. The spectral resolution, as measured from the widths of the night skylines, was 5300 ± 300 for the observations with the $0''.85$ width slit, and 4700 ± 200 for the observations with the $1''$ width slit.

The data were reduced as described in Rigby et al. (2018).

2.4. X-Ray Observations

The field containing the Sunburst Arc was observed with the Chandra X-ray Observatory under observation ID 20442 (PI: Bayliss). The purpose of these observations was to test for the presence of an X-ray bright AGN as a possible source of ionizing radiation in the lensed galaxy. The observations consisted of a single 39.53 ks exposure, with the aimpoint located near the center of the I3 chip in the ACIS-I array in VFaint telemetry mode. All Chandra data reductions and analyses were performed using the Chandra Interactive Analysis of Observations (CIAO v4.13), with CALDB v4.9.6. We reprocessed the data using the CIAO

Table 1
Observation Log for Magellan/FIRE

FIRE Slit	MagE Slit	R.A.	Decl.	UT Date	Time (ks)	LyC Leaker	z_{spec}	PA	Magnification(μ)
F-0	M-0	15:50:04.317	-78:10:59.87	2016 Mar 30	3.6	Yes	2.37014	140.2	$7.8^{+15}_{-5.9}$
F-1	...	15:50:06.008	-78:10:58.07	2017 Mar 28	3.6	Yes	2.37009	30.2	$40.3^{+1.0}_{-4.7}$
F-2	M-2	15:49:59.662	-78:11:13.48	2017 Mar 28	3.6	Yes	2.37017	100.2	$30.7^{+6.1}_{-2.9}$
F-3	M-3	15:50:00.488	-78:11:10.00	2017 Mar 28	4.8	No	2.37025	125.2	$36.7^{+4.5}_{-4.9}$
F-4	M-4	15:50:04.824	-78:10:59.20	2017 Mar 29	3.6	No	2.37073	140.2	$14.7^{+0.7}_{-2.6}$
F-5	M-5	15:50:01.005	-78:11:08.07	2017 Mar 29	2.7	No	2.37086	165.2	$49.4^{+5.0}_{-11.3}$
F-6	M-6	15:50:06.557	-78:10:57.52	2017 Mar 29	2.7	No	2.37021	32.2	$141.0^{+35.0}_{-27.0}$
F-7	M-7	15:50:07.238	-78:10:57.22	2017 Mar 29	2.7	Yes	2.37044	20.2	$34.4^{+2.4}_{-5.6}$
F-8	M-8	15:49:59.834	-78:11:12.48	2017 Aug 28	3.6	Yes	2.37024	100.2	$28.9^{+6.1}_{-2.9}$
F-9	M-9	15:50:00.251	-78:11:10.71	2017 Aug 27	5.4	Yes	2.37030	100.2	$30.9^{+3.8}_{-3.2}$

Note. Column 1: FIRE slit names. Column 2: the closest corresponding MagE slit names. Column 3: right ascension (J2000). Column 4: decl. (J2000). Column 5: universal date, universal time. Column 6: the integration time in kiloseconds. Column 7: whether that source is a LyC leaker, according to the HST F275W imaging. Column 8: spectroscopic redshift, measured from optical lines. Column 9: the position angle (degrees east of north) of the FIRE slit. Column 10: the average magnification factor (μ) within the slit.

chandra_repro routine, and filtered the data for flares using the `lc_sigma_clip` function in the `lightcurves` Python package that is included in CIAO. The resulting “clean” integration time was 38.53 ks. We applied an energy filter of 0.5–7 keV, visually identified bright sources in the data, and performed an initial background estimation by masking out those visually identified sources. We then ran the `wavdetect` procedure, using the initial background estimate to identify point sources in the data. We then masked the point sources and the bright emission from the galaxy cluster responsible for lensing the Sunburst Arc, and used the resulting “source-free” data to perform a final measurement of the background statistics.

3. Methods

3.1. Stacking the MagE and FIRE Spectra

As demonstrated in Rivera-Thorsen et al. (2019), all the LyC leaking regions in the image plane that were targeted with Magellan/FIRE and Magellan/MagE are in fact multiple images of a single physical region in the source plane. It is therefore appropriate to combine the spectra from these “leaker” slits, since they arise from the same physical source. By contrast, the four slits that target nonleaking regions (see Figure 1) correspond, according to the lens model, to at least seven different physical regions. While it is desirable to study these regions separately, for some applications stacking is a practical necessity, as the surface brightness of the nonleaking regions is low. As such, we separately stacked the spectra of the LyC leaking regions and the nonleaking regions, to study the characteristic differences.

The FIRE stacking was conducted as follows. As shown in Table 1, six FIRE slits (F-0, F-1, F-2, F-7, F-8, and F-9) cover the LyC leaker, and four slits (F-3, F-4, F-5, and F-6) cover the nonleaking regions. Of the four slits covering the nonleaking regions, we exclude slit F-3 for further analysis, since this region may contain an atypical extragalactic object (Vanzella et al. 2020). The remaining spectra are then normalized by their respective [O III] λ 5007 flux density. We then perform average stacking of the FIRE spectra of the six LyC leaker slit positions and the three nonleaking slit positions. Figure 2 shows the resulting stacked FIRE spectra.

We also produced stacked rest-frame UV spectra of the LyC leaker and the nonleaking regions. All but one of the FIRE slits (i.e., F-1) have corresponding MagE spectra. We also excluded the MagE spectrum corresponding to the FIRE F-3 position (i.e., M-3) for further stacking analysis, resulting in five leaker spectra (M-0, M-2, M-7, M-8, and M-9) and three nonleaker spectra (M-4, M-5, and M-6). Since all the LyC leaker images are of the same physical star-forming region (Rivera-Thorsen et al. 2019), leaving this one leaker region (compared to the FIRE stack) wouldn’t have any impact on the stacked spectrum aside from slightly lowering the signal-to-noise ratio (S/N). We then normalized all the leaker and nonleaker spectra with their continuum flux densities from the rest frame to 1500 Å. After normalization, we performed average stacking to produce the stacked rest-frame UV spectra for leakers and nonleakers. Figure 3 shows the stacked rest-frame UV spectra of the leakers (blue) and the nonleakers (red).

3.2. Emission Line Fitting in the FIRE Spectra

The complex emission line profiles shown in Figure 2 require two Gaussian components for each emission line. We fit the observed emission line profiles by assuming that all the emission lines can be fit by the same number of components at the same velocity, but with varying total fluxes. We fixed the line flux ratio of [O III] λ 5007,4959 to 3.01 (Storey & Zeppen 2000). We identified [O III] λ 5007 as the highest-S/N emission line that is not impacted by any sky residual. We fit [O III] λ 5007 with a two-component Gaussian model, and identify the systemic redshift traced by the narrow component.

For all the other emission lines, we fixed the systemic redshift as well as the line widths of two Gaussian components traced by [O III] λ 5007 (after accounting for instrument resolution). We also fixed the relative offset between the two components, as given by the [O III] λ 5007 line profile. However, we set the narrow-to-broad component integrated flux ratio to be a free parameter. The measured emission line fluxes from the two-component Gaussian model are given in Table 2, for both the leaker and the nonleaker stacks.

3.3. Systemic Redshift

The best published systemic redshift for the Sunburst Arc, 2.3709 ± 0.001 , comes from a stellar population fitting to the

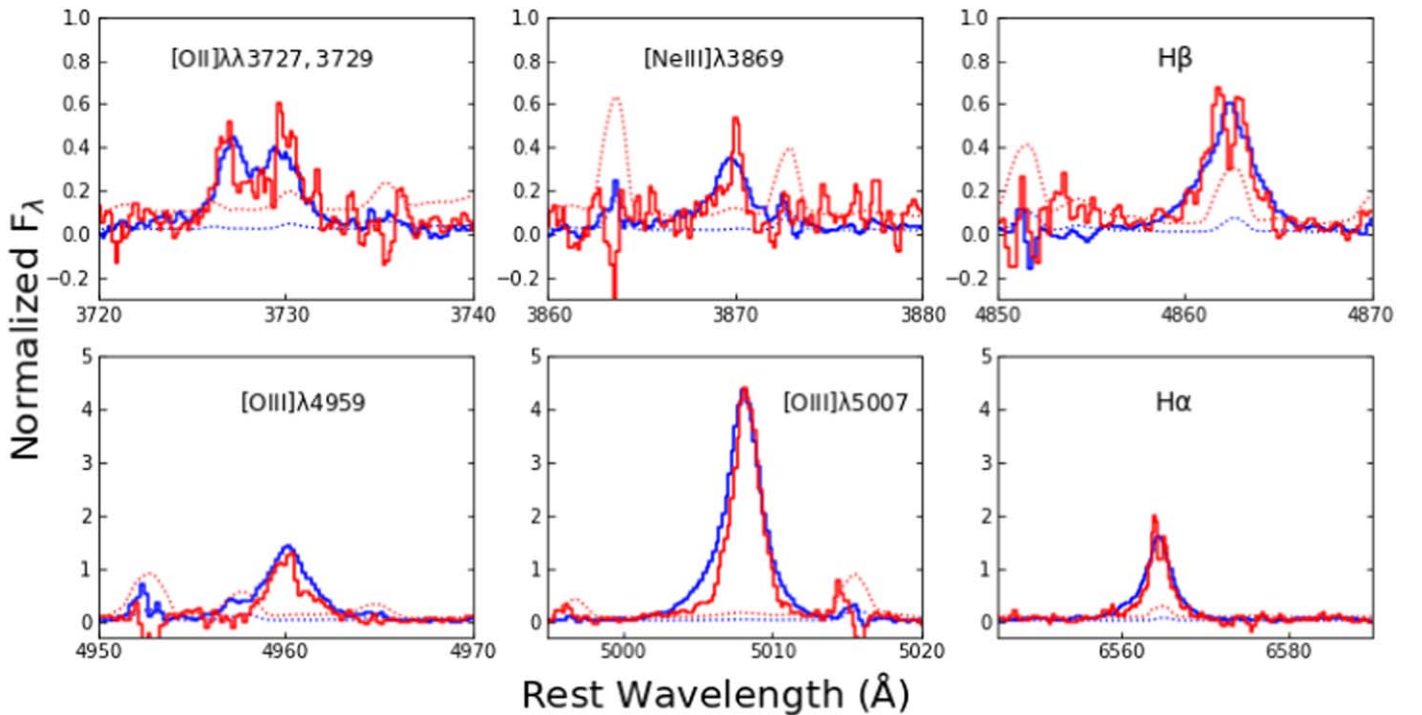


Figure 2. Magellan/FIRE spectra (normalized by [O III] λ 5007) showing the key spectral features in the stacked spectra of the LyC leaking regions (blue) and nonleaking regions (red). The corresponding error spectra are shown in the dotted blue lines (leaker) and the dotted red lines (nonleaker).

MagE M-0 spectrum (Chisholm et al. 2019). The high S/N of the emission lines in the FIRE data potentially enables a more precise measurement. We measured the velocity centroids of the narrow components of the brightest line, [O III] λ 5007, in each FIRE pointing. The resulting redshifts are given in Table 1. The average redshift from the [O III] λ 5007 emission is 2.37034 ± 0.00024 , consistent with the previous result.

3.4. Stellar Population Fitting to the MagE Spectra

The rest-UV spectra contain several key features that indicate the age and metallicity of the massive stellar population. The stellar population fitting of the stacked spectra followed the procedure described in Chisholm et al. (2019). To summarize: we assume that the spectra can be fit by a linear combination of bursts of stellar populations, each with a given age and metallicity, with a single reddening $E(B-V)$ value. For the theoretical stellar models, we considered single-star Starburst99 models (Leitherer et al. 1999, 2010, 2014). We assume a Kroupa initial mass function (Kroupa 2001), with a broken power law with a high- (low-) mass exponent of 2.3 (1.3) and a high-mass cutoff of $100 M_{\odot}$. We then propagated the intrinsic spectra through a uniform dust screen, using the Reddy et al. (2016) attenuation law. We fit the observed spectra between rest-frame wavelengths of 1220 Å to 2000 Å. The outputs of this process are the linear coefficients for each of the 50 single-age, single-metallicity models, as well as an $E(B-V)$ reddening value.

3.5. Lensing Magnification

We define pixel-level masks that identify the FIRE slit positions along the giant arc from the available HST imaging by flagging which pixels fall inside or outside each observed FIRE slit position. Only pixels that have more than half of their

area falling within the slit aperture are counted as being inside the slit, and any effects from fractional slits should be extremely minor, considering the small pixel size ($0''.03$) in our drizzled HST images relative to the FIRE slit size. The slit definition masks are then used to define an aperture mask for each position, which represents the intersection of the FIRE slit aperture and the emission from the giant arc. These apertures represent HST pixel-level masks that indicate the regions on the sky from which light entered the FIRE slit at each position listed in Table 1.

For the purpose of defining these apertures, we use HST F125W (the band closest to the J band used in the FIRE acquisition camera). We compute the sky background statistics in F125W and manually mask out any other sources that have fallen into some of the slits. We then define the emission from the giant arc as originating from all pixels within a given FIRE slit that are $8\sigma_{\text{sky}}$ above the sky background level. We experimented with several different integer multiples of σ_{sky} as the threshold, and found that $8\sigma_{\text{sky}}$ strikes a good balance between robustly identifying the giant arc emission without including spurious sky pixels, while also capturing the large majority ($\gtrsim 90\%$) of the total giant arc flux in each slit.

The average magnification within each aperture is determined as follows. We first ray-trace each aperture from the image plane to the source plane, using the lens model deflection map outputs. We then calculate the area enclosed by the aperture in the source plane and in the image plane. The average magnification is defined as the ratio of the image plane to the source plane areas.

Some of the apertures cross the critical curves and include portions of the arc that traverse it, causing the source plane projection of the aperture to fold over itself (see, e.g., Figure 6 of Sharon et al. 2012 for an illustration of this behavior). Therefore, care must be taken in deriving their average

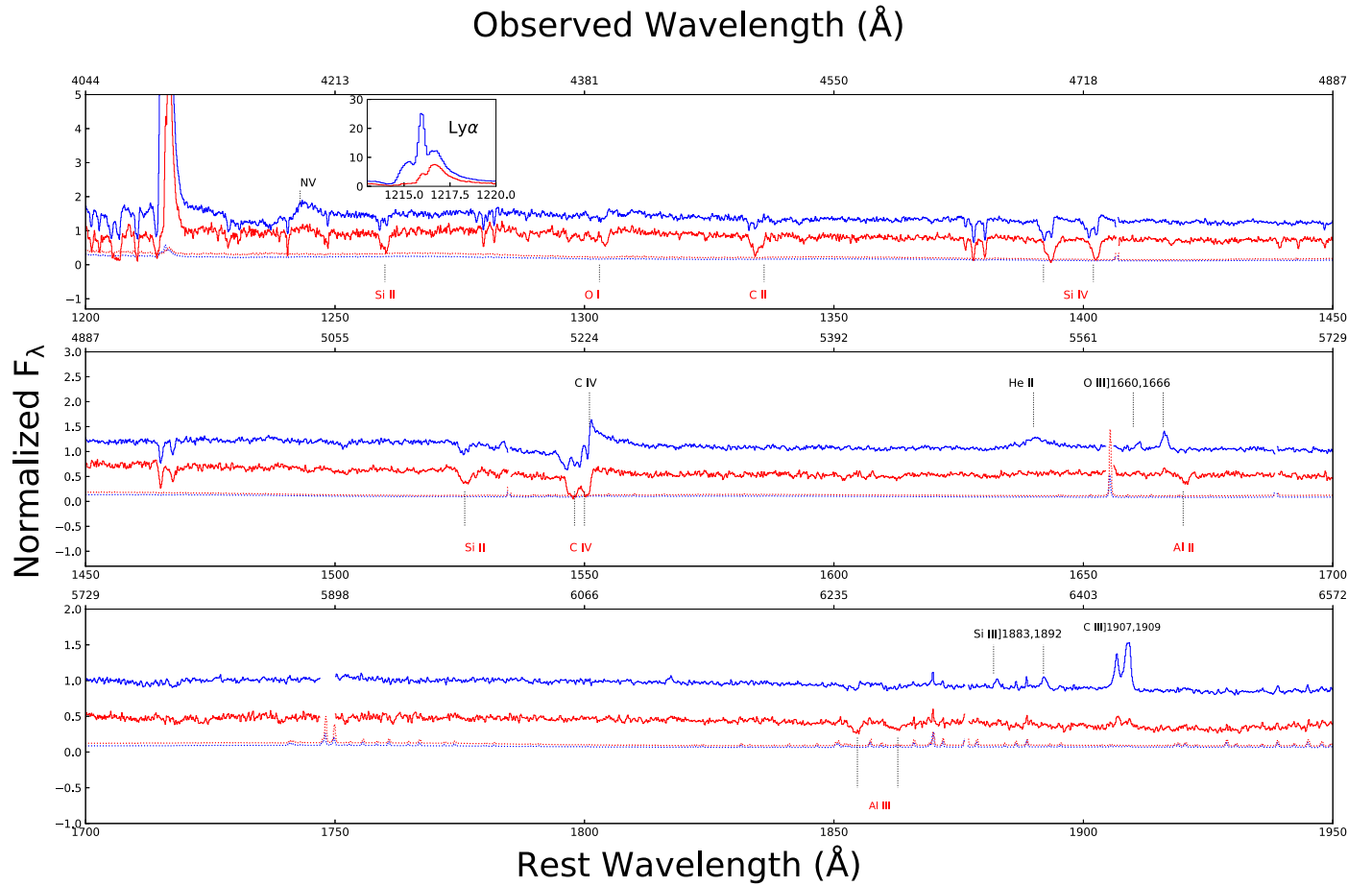


Figure 3. Magellan/MagE spectra showing the stacked spectra of the LyC leaking regions (blue) and the nonleaking regions (red). The leaker spectrum is normalized by a median continuum level between 1400 and 1500 Å, while the nonleaker spectrum is further offset by 0.5, for clarity of plotting. The corresponding error spectra are shown by the dotted blue line (leaker) and the dotted red line (nonleaker). The figure shows several emission (black label) and absorption (red label) features. The emission lines are more prominent in the leaker spectrum, while the absorption lines, particularly low-ionization interstellar features (see Section 3 for more details), are prominent in the nonleaker spectrum.

Table 2

Two-component Gaussian Fits to the Stacked FIRE Spectra of the LyC Leaker and Nonleaker

Line	Leaker		Nonleaker	
	Narrow	Broad	Narrow	Broad
[OII] 3727	4.9 ± 0.2	4.5 ± 0.3	0.6 ± 0.1	0.6 ± 0.2
[OII] 3729	5.3 ± 0.2	4.8 ± 0.3	0.8 ± 0.1	0.8 ± 0.2
[NeIII]3869	3.0 ± 0.2	7.5 ± 0.4	0.5 ± 0.3	0.7 ± 0.9
H β	6.8 ± 0.3	14.2 ± 0.4	1.5 ± 0.2	1.5 ± 0.4
[OIII] 5007	64.8 ± 0.3	77.8 ± 0.4	12.2 ± 0.1	4.3 ± 0.3
H α	27.1 ± 0.5	47.1 ± 0.6	5.6 ± 0.2	3.9 ± 0.3
[NII] 6584	<0.6	<1.1	<0.3	<0.6

Note. The table shows the line fluxes in both the narrow and broad emission components. The line fluxes are given in units of 10^{-17} erg s $^{-1}$ cm $^{-2}$.

magnification. In such cases, the overlapping region in the source plane should only be counted once, with the average magnification accounting for the fact that the slit aperture encloses two images of the same source region.

Magnification uncertainties are estimated by running the same process on the deflection maps calculated from sets of parameters in the Markov Chain Monte Carlo that sample 1σ in the parameter space. The resulting magnifications and their uncertainties are tabulated in Table 1.

4. Results

4.1. Nebular Reddening

We apply a nebular reddening correction using the Balmer lines (H α and H β) measured in the leaker stacked spectra. While H β is slightly impacted by an underlying skyline in the individual spectra, we successfully recover it in the stacked spectra. We use the observed H α /H β line ratio of 3.533, and first apply a Milky Way extinction correction, using $E(B-V) = 0.094$ (Green et al. 2015). In the next step, we assume Case B recombination, to infer an intrinsic value of $(H\alpha/H\beta)_{\text{in}} = 2.86$, corresponding to a temperature of $T = 10^4$ K and an electron density of $n_e = 10^2$ cm $^{-3}$. For the extinction law of Cardelli et al. (1989) and an R_V value of 3.1, this corresponds to a nebular reddening of $E(B-V) = 0.195 \pm 0.025$. Recovering a reliable H β measurement in the nonleaker stack is challenging for two reasons. First, nonleaking regions have lower surface brightness, and hence lower S/Ns, in the individual emission lines. Second, only three spectra are stacked for the nonleaker (compared to six for the leaker), again resulting in lower-S/N emission lines. This prevents us from estimating a reliable H α /H β ratio for the nonleaker. We therefore assume that the nebular reddening value of the leaker is representative of the whole Sunburst Arc.

Table 3Derived $E(B-V)$ Reddening, Stellar Metallicity, and Stellar Age from the Stellar Population Fits to the MagE Data for the Sunburst Arc

MagE Slit	$E(B-V)$	σ	Metallicity (Z_*/Z_\odot)	Age (Myr)
M-0*	0.146	0.003	0.55	2.92
M-2*	0.059	0.003	0.50	3.04
M-3	0.018	0.003	0.23	4.03
M-4	0.078	0.005	0.36	10.1
M-5	0.054	0.004	0.24	12.4
M-6	0.080	0.004	0.28	11.3
M-7*	0.098	0.007	0.40	2.60
M-8*	0.040	0.002	0.40	2.65
M-9*	0.049	0.005	0.44	2.84

Note. The asterisks denote the MagE slits targeting LyC leaking regions.

4.2. Stellar Reddening

The stellar reddening is inferred by fitting the rest-frame UV MagE data (see Section 2.4). These results are given in Table 3, and cover a larger range of physically distinct regions than is currently available for the reddening data. We therefore use this stellar reddening information to check whether there are large spatial gradients in the reddening. The results presented in Table 3 show no apparent trend of $E(B-V)_*$ with whether the slit covers the leaking or the nonleaking regions. This supports the validity of using a single nebular reddening value for the whole of the Sunburst Arc.

4.3. Comparison of UV Features in Leaking and Nonleaking Regions

Figure 3 plots the MagE spectra for the leaker and the nonleaker. The two spectra are quite different in several ways. First, as shown in the figure inset, the Ly α velocity profiles are radically different. The leaker shows a triple-peaked profile, which is a characteristic feature of ionizing photons leaking from the galaxy. This feature is clearly absent from the nonleaker stacked spectra. More specifically, the nonleaker lacks the blueshifted Ly α emission, which would suggest that the line-of-sight ISM is sufficiently neutral for absorbing Ly α photons. This confirms, with deeper data, the results seen by Rivera-Thorsen et al. (2017).

Second, the rest-frame UV nebular emission lines—namely C III] $\lambda\lambda$ 1907, 1909, O III] $\lambda\lambda$ 1661, 1666, and Si III] $\lambda\lambda$ 1883, 1892—have much larger EWs in the leaker stack than in the nonleaker stack. These features are characteristics of galaxies that are dominated by young massive star populations (Stark et al. 2013; Berg et al. 2016; Du et al. 2018; Rigby et al. 2021).

Third, the spectral wind features that are characteristic of massive stars are much stronger in the leaker than in the nonleaker. These features are described in detail in Chisholm et al. (2019). Figure 4 compares these features for the leaker and the nonleaker—namely, the N V, C IV, and He II emissions. In particular, the leaker shows strong P-Cygni N V and C IV emission, which is characteristic of an extremely young (2–5 Myr) stellar population. In contrast, these features are very weak in the nonleaker (Figure 4). The leaker shows C IV emission, both a narrow component and a broad component, which again are characteristic of massive star winds. The narrow component is likely nebular emission, which is commonly detected in LyC emitting sources (e.g., Naidu et al. 2022; Schaerer et al. 2022). C IV also shows the

Table 4

Table Showing Optical Line Diagnostic Ratios (Combined Broad and Narrow) for the Leaker and Nonleaker Stacks

Line Ratios	Leaker	Nonleaker
O32	7.5 ± 0.9	6.1 ± 1.9
[OIII]5007/H β	6.6 ± 0.8	5.3 ± 1.5
R23	9.4 ± 1.1	8.3 ± 2.3
[NII]6584/H α	<0.002	<0.009

Note. The limits are 3σ .

blueshifted absorption that is characteristic of stellar winds. These features are much weaker in the nonleaker. Additionally, the leaker shows broad He II emission that is entirely absent from the nonleaker. This is only found in massive Wolf–Rayet stars, and must indicate that there has been a very recent burst of star formation. Together, these spectral features indicate a very different light-weighted age for the leaker stack compared to the nonleaker stack, which we now quantify.

4.4. Stellar Age and Metallicities

The stellar population synthesis fits use both the strong stellar wind lines (such as N V and C IV) and the weak stellar photospheric absorption features to match the observations as best-fit stellar templates. Using this information, the fittings estimate a UV light-weighted age of 3.3 ± 0.5 Myr and a metallicity of $0.46 \pm 0.06 Z_\odot$ for the leaking region, with 11.8 ± 0.9 Myr and $0.30 \pm 0.05 Z_\odot$ for the nonleaking region.

As discussed in Section 4.3, Figure 4 compares the observations (in black) to the data (in gold) for the leaker (upper panel) and nonleaker (lower panel) spectra. The left and middle panels show that the stellar population fits to the strong N V and C IV stellar wind lines. These wind lines display the classic P-Cygni wind feature, with blueshifted absorption and redshift emission arising from the gas launched off the photospheres of massive stars. While both the leaking and nonleaking fits match the absorption components, the C IV feature for the leaker shows evidence of narrow C IV emission, which is not well fit by the model. The He II region is well fit in the nonleaker case, but poorly fit in the leaker case. This is due to the broad (~ 2000 km s $^{-1}$) emission seen in the leaker spectrum. Broad He II emission is typically seen in massive, moderately metal-rich Wolf–Rayet stars with very young ages. Thus, the observed broad He II is consistent with the young estimated age of the leaker region, and the absence of broad He II from the nonleaking region is consistent with an older fitted stellar population. The fact that the Starburst99 models do not match the He II feature is a common problem in the current generation of stellar models, because the stellar tracks do not populate the Wolf–Rayet stars that produce this feature (Leitherer et al. 2010; Chisholm et al. 2019). Thus, the dichotomy of stellar properties—a young and moderately metal-rich population in the leaking region, with an older population in the nonleaking region—is consistent with the observed stellar features.

4.5. Rest-frame Optical Diagnostic Line Ratios

The rest-frame optical strong emission lines form the classic line ratio diagnostics that are used to classify galaxies as dominated by star formation or active nuclei, and that are sensitive to the metallicity and ionization state of the nebular

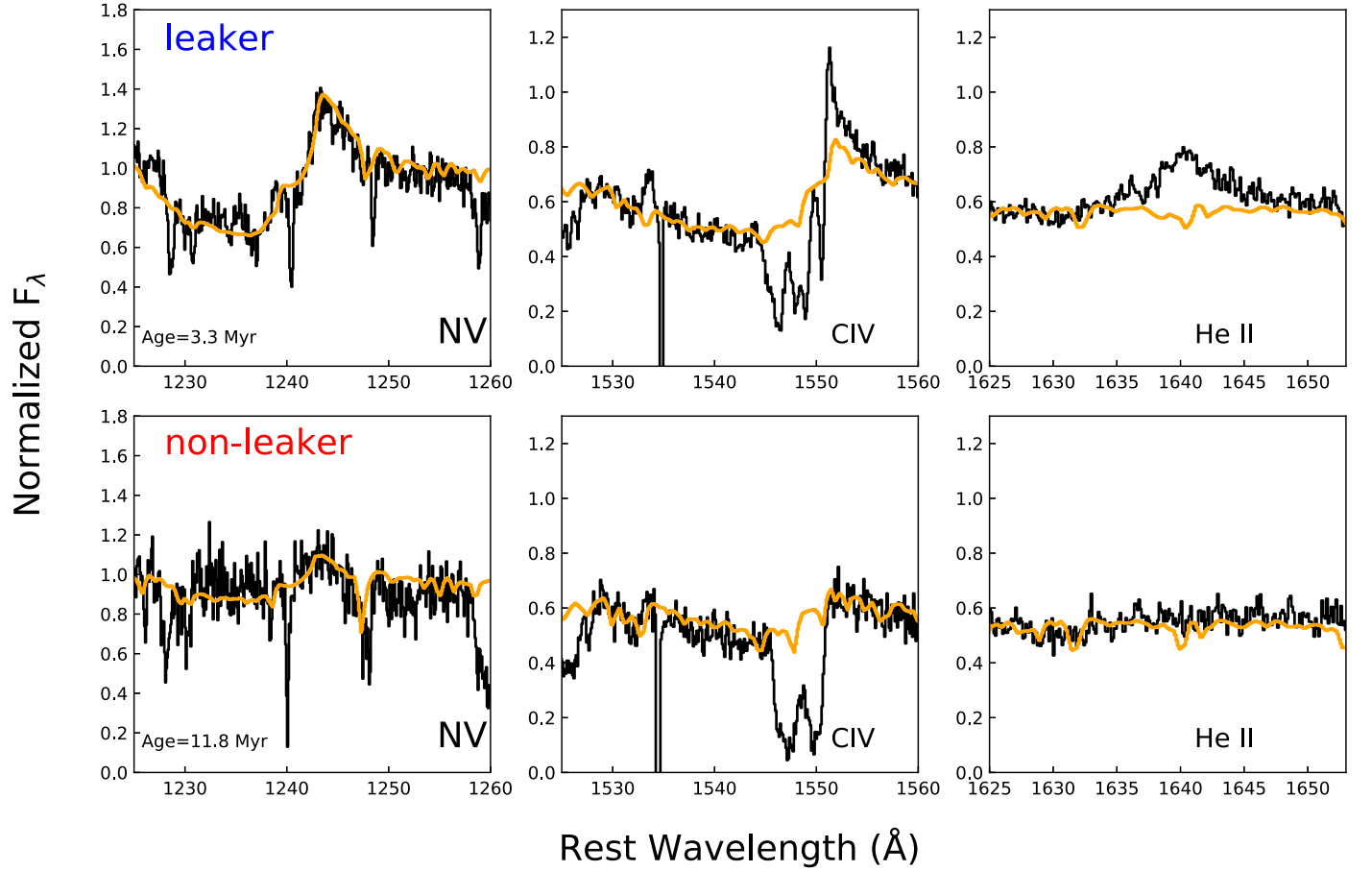


Figure 4. Stellar population synthesis fits to the leaker and nonleaker spectra. The left panels show P-Cygni N v features in the leaker (top) and the nonleaker (bottom); the middle panel shows P-Cygni C iv features in the leaker (top) and the nonleaker (bottom); and the right panel shows He II 1640 features in the leaker (top) and the nonleaker (bottom). The orange line represents the best-fit light-weighted Starburst99 model: the inferred ages are 3.3 Myr for the leaker and 11.8 Myr for the nonleaker.

gas. In Table 4, we report the measured values for the standard emission line ratios (for combined broad and narrow components), after accounting for the internal extinction discussed above. Both the leaker and nonleaker show larger than average O32 and $[\text{O III}]\lambda 5007/\text{H}\beta$ for typical $z \sim 2$ galaxies, suggesting that the galaxy is in a higher ionization state compared to typical galaxies at similar redshift (Sanders et al. 2016; Steidel et al. 2016). O32 is often thought of as a proxy for LyC escape (e.g., Jaskot & Oey 2013; Nakajima & Ouchi 2014), but it is often not seen to scale with LyC escape at low redshift (Izotov & Thuan 2008; Flury et al. 2022a). Interestingly, these line ratios are not very different for the individual leaker and nonleaker stacks. We note that the nonleaker stack does not include all the nonleaking regions identified in the Sunburst Arc.

In Figure 5, we plot the classic BPT diagram (Baldwin et al. 1981), in an $[\text{O III}]\lambda 5007/\text{H}\beta$ versus $[\text{N II}]\lambda 6583/\text{H}\alpha$ plot. The gray data points indicate Sloan Digital Sky Survey (SDSS) galaxies ($z \sim 0$), the green circles indicate $z \sim 2.3$ galaxies from the MOSDEF survey (e.g., Sanders et al. 2016), and the dotted line indicates the AGN versus star-forming galaxies classification, based on the Kauffmann et al. (2003) model. The line flux ratios of both the leaker (blue) and the nonleaker (red) are shown in the diagram. Since $[\text{N II}]$ is not detected in either stack, we only have limits on the $[\text{N II}]/\text{H}\alpha$ ratio, but these limits tightly constrain both the leaking and nonleaking portions of the Sunburst Arc to the far upper left wing of the

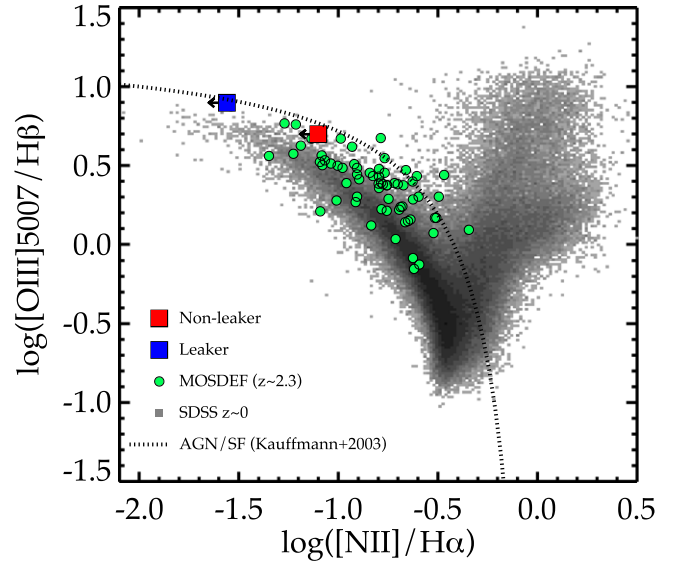


Figure 5. The ionization diagram showing the location of the leaker (blue) and the nonleaker (red), using combined broad and narrow components. The gray squares represent SDSS data points and the green circles are $z \sim 2.3$ galaxies from the MOSDEF survey (Sanders et al. 2016). The dotted line represents the AGN/star formation demarcation from Kauffmann et al. (2003).

“seagull”-shaped cloud that the SDSS galaxies inhabit. Both the leaker and nonleaker stacks show high $[\text{O III}]\lambda 5007/\text{H}\beta$, distinct from the typical star-forming galaxies in the SDSS sample.

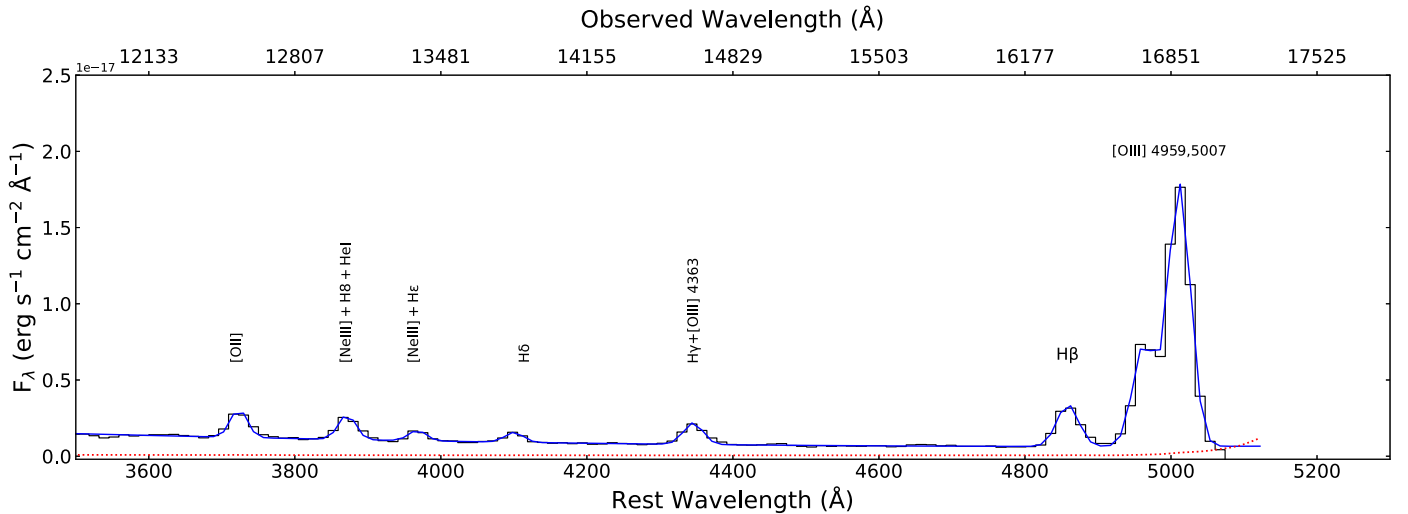


Figure 6. HST WFC3/IR G141 grism spectrum of a LyC leaking region (knot 3) in the Sunburst Arc. The black line represents the grism spectrum, the dotted red line shows the noise level, and the blue line shows the best fit to the data.

Table 5
HST Grism Measurements of the LyC Emitting Region (Knot 3)

Line	[O II]	[Ne III] + H8 + He I	[Ne III]+He	H δ	H γ + [O III]4363	H β	[O III]4959	[O III]5007
Flux	19.2 ± 1.3	19.3 ± 4.0	7.5 ± 2.2	7.4 ± 1.9	19.5 ± 4.8	36.6 ± 2.0	80.5 ± 0.7	242.5 ± 2.1
EW (Å)	46.7 ± 3.1	52.8 ± 10.9	22.0 ± 6.5	42.1 ± 6.2	74.7 ± 18.4	169.9 ± 9.3	373.4 ± 3.2	1119.7 ± 9.7

Note. The line fluxes and uncertainties are given in units of 10^{-17} erg s $^{-1}$ cm $^{-2}$.

However, such a high [O III]/H β is consistent with the young metal-poor galaxy population that is typically observed at intermediate redshifts (e.g., Vanzella et al. 2017; Berg et al. 2018; Mainali et al. 2020).

4.6. X-Ray Constraints on AGNs

We search for X-ray emission from the lensed Sunburst Arc to look for direct evidence of any possible AGNs that could be contributing substantially to the ionizing radiation in the galaxy. We define an aperture for the Chandra data by convolving the Chandra point-spread function with contours that trace the optical emission of the Sunburst Arc in the HST imaging. The bright extended X-ray emission from the foreground lensing galaxy cluster overlaps with the location of the lensed images of the Sunburst Arc, effectively acting as another source of background noise for the purpose of constraining the emission from the arc. To account for the X-ray photons from the cluster, we fit a radially symmetric β -profile to the cluster emission. We use the model to subtract off the cluster emission underneath the giant arc aperture, resulting in a measurement of the X-ray emission from the Sunburst Arc; the result is a nondetection of the giant arc, with a 0.5–7 keV 2σ limiting flux of 6.6×10^{-15} erg s $^{-1}$ cm $^{-2}$. Assuming a power-law spectra shape with $\Gamma = 1.8$ (which is reasonable for AGNs), this corresponds to a rest-frame 2–10 keV flux limit of 3.6×10^{-15} erg s $^{-1}$ cm $^{-2}$ at $z = 2.37$, and an upper limit on the intrinsic 2–10 keV luminosity of $L_{2-10} < 1.6 \times 10^{44}$ erg s $^{-1}$. These limits do not account for the lensing magnification, which reduces the constraint on the upper limit by the magnification, μ . We estimate the median magnification factor based on our strong lensing model of the Sunburst Arc system by using the full aperture within which the Chandra upper limit was measured; the resulting magnification is $\mu \simeq 38$. Applying

this magnification factor to the upper limit on the X-ray luminosity constrains the intrinsic X-ray luminosity of the Sunburst Arc to $L_{2-10} \lesssim 7.6 \times 10^{42}$ erg s $^{-1}$, ruling out the presence of an X-ray bright AGN in the Sunburst Arc.

4.7. EWs of the Rest-frame Optical Emission Lines

The EWs of the nebular emission lines tell us about the relative strengths of the nebular emission compared to the stellar emission. Because it is a ratio, it is not affected by lensing magnification. It therefore tells us about the intensity and age of the massive stellar population. The nondetection of continuum in the FIRE data precludes us from obtaining a reliable EW measurement, but we can measure them using the grism data.

We plot the leaker spectrum in Figure 6 and present the measurements in Table 5, while a similar measurement for the nonleaker spectrum is not currently possible with the grism data. This is because continuum is weakly detected in the nonleaker, owing to its lower surface brightness, and is further contaminated by nearby star lights. For the leaker, the EWs are very high, which is typical of LyC emitting galaxies (e.g., Izotov et al. 2018; Flury et al. 2022b). Such large EWs are also commonly observed among extreme emission line galaxy populations (Labbé et al. 2013; Amorín et al. 2017; Mainali et al. 2020; Berg et al. 2021).

4.8. Evidence for Ionized Outflows in the Stacked Spectra

The strongest optical emission line in the FIRE data is [O III] $\lambda 5007$, which is also free of contamination from telluric skylines. Examining Figure 2, it is immediately obvious that the stacked leaker and the stacked nonleaker FIRE spectra show very different velocity profiles for [O III] 5007. The

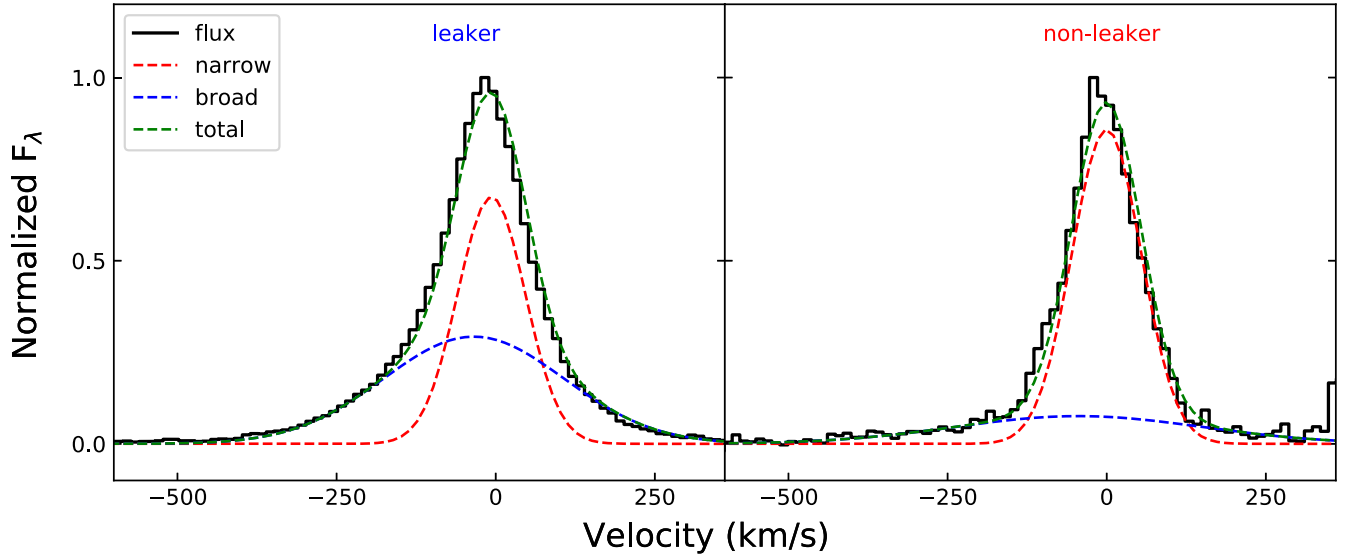
[O III] λ 5007 Velocity Profile

Figure 7. [O III] λ 5007 emission line profile in leaking (left) and nonleaking (right) regions. The black curve represents the FIRE spectra. We fit the data with a two-component Gaussian model, where the dashed red line represents the narrow component and the dashed blue line represents the broad line. The dashed green line represents the best-fit model.

Table 6
Breakdown of the Narrow and Broad Components in the Leaker versus the Nonleaker, Measured from [O III] λ 5007 Emission

	Centroid (Narrow) km s ⁻¹	FWHM (Narrow) km s ⁻¹	Centroid (Broad) km s ⁻¹	FWHM (Broad) km s ⁻¹	Fractional Light in Broad Component %
Leaker	0	112 ± 1	-27 ± 1	326 ± 2	54.5 ± 0.3
Nonleaker	0	115 ± 2	-43 ± 14	454 ± 47	26.1 ± 7.0

leaker stack shows a strong broad wing of emission, which is considerably weaker in the nonleaker stack. The leaker stack also shows a broad red wing.

Table 2 reports the relative fluxes of the broad and narrow components for both the leaker stack and the nonleaker stack. Figure 7 shows in detail the best-fit broad and narrow components of the [O III] λ 5007 velocity profile. The observed line widths (FWHMs) of the narrow component and the broad component in the leaker are ~ 112 km s⁻¹ and ~ 326 km s⁻¹. The broad emission is blueshifted from the narrow component by $\Delta V = 27$ km s⁻¹. For [O III] 5007, $54.5\% \pm 0.3\%$ of the line flux is in the broad component for the leaker stack, with $26.1\% \pm 7.0\%$ for the nonleaker stack. The measurements are given in Table 6.

Though it suffers from some skyline contamination (particularly in the nonleaker stack), the H α velocity profiles tell the same story: the leaker stack shows a broad blue wing that is much stronger than in the nonleaker stack. H α also appears to have a higher fraction of flux in the broad component compared to the [O III] 5007 line ($63.4\% \pm 1.5\%$ and $41.1\% \pm 9.3\%$ for the leaker and the nonleaker, respectively).

4.9. Evidence for Ionized Outflows in the Individual Spectra

The above analysis was performed on the stacked FIRE spectra. Each individual spectrum that makes up the stacked leaker spectra is intrinsically the same source, multiply imaged. There is therefore no value in analyzing the kinematics of each

Table 7
Distinct Physical Regions of the Sunburst Arc Targeted by the FIRE Spectra (Sharon et al. 2022)

FIRE Slits	Physical Regions	Distance (kpc)
F-0	1	0
F-4	3, 4, 7, 9, 10	1.53 ^{+0.50} _{-0.23}
F-5	3, 8	1.06 ^{+0.20} _{-0.11}
F-6	2	0.47 ^{+0.03} _{-0.07}

Note. Column 1: the FIRE slit name. Column 2: the distinct physical regions within the FIRE pointing. Column 3: the average distance (pc) of the physical regions from the LyC emitting region in the source plane.

individual leaker spectrum. By contrast, the nonleaker stack is comprised of six different physical regions, based on the lens model (Sharon et al. 2022), even though only four FIRE slits target nonleaking regions. This is because a FIRE slit may target several unresolved physical regions. The leaker FIRE spectrum F-0 targets Clump 1, while the nonleaker spectrum F-4 targets Clumps 2, 3, 4, 9, and 10, F-5 targets Clumps 3, 8, and 10, and F-6 targets Clump 2 (Table 7). We therefore further examine the [O III] 5007 in the individual (nonstacked) nonleaker FIRE spectra to study any spatial variation in the line profile. We calculate angular separations in the object planes for different star-forming clumps in the leaker and nonleaker spectra. We then convert them to the average distance (in parsecs) from the leaking region to the regions targeted by F-4, F-5, and F-6 (see Table 6).

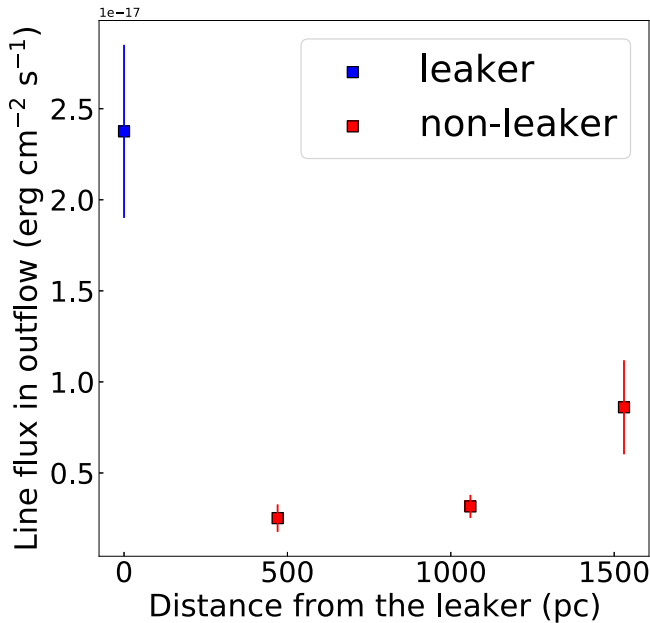


Figure 8. Intrinsic line flux (magnification-corrected) of the outflow component measured from the broad component in the [O III] 5007 line for the leaker (the blue square) and three individual nonleakers (the red squares) probed by the FIRE slits. On the x -axis, we plot the physical distances between the leaker and the three nonleakers in the source plane, as given by the lens model (Sharon et al. 2022).

In Figure 8, we show the intrinsic line flux in the broad component of the [O III] 5007 line as a function of the average distance from the leaker. The intrinsic line flux is obtained after applying the magnification correction presented in Table 1 to the observed line fluxes. Clump 2 (400 pc from the leaker) lies very close to the critical curve in the source plane, resulting in extremely large magnification ($\mu = 637$). This implies an intrinsically negligible flux contribution from Clump 2. While we see a broad outflow component in every physical region, the figure demonstrates that the ionized gas outflow is strong in the leaker, and that it is weak at the 0.5–1 kpc distances probed by the FIRE pointings that cover nonleaking regions.

4.10. The Outflow as Traced in Absorption of Low-ionization and High-ionization Gas

The rest-UV stacks shown in Figure 3 show several interstellar absorption features, which tell us about the line-of-sight absorbing gas kinematics. These absorption features are blueshifted with respect to the systemic velocity, which indicates the presence of outflowing gas, consistent with the outflows traced in the emission lines discussed above. While the flux in the emission lines depends on n_e^2 , the outflows traced by the line-of-sight absorption scale as n_e . Absorption is more sensitive to gas at larger distances and gas with lower densities. Thus, the absorption lines probe different physical regions of outflow than the emission lines. The absorption lines also have sensitivity to a range of ionization states.

In Figure 9, we show the different interstellar absorption features identified in the leaker and nonleaker stacks, and compare them with the gas kinematics observed with the [O III] 5007 line. The resolution of the MAGE spectra provides resolved velocity profiles of the interstellar absorption lines. We normalize the spectra using the continuum level obtained

from the stellar population fitting procedure, as discussed in Section 3.4.

For the nonleaker, the stacked MagE spectra show prominent absorption from low-ionized gas (Si II 1260, O I 1302, C II 1334, and Al III 1670). The absorption peaks at ~ -150 km s⁻¹ relative to systemic, and extends from $\sim +50$ to ~ -500 km s⁻¹. The highly ionized gas, as traced by Si IV and C IV, shows similar gas kinematics.

By contrast, for the leaker, the stacked MagE spectra show extremely weak absorption from the same four tracers of low-ionized gas. A small amount of blueshifted absorption appears at ~ -50 km s⁻¹ and ~ -375 km s⁻¹ relative to systemic. The high-ionization transitions show strong absorption at these same two velocities and, in addition, show a tail of high-velocity absorption extending out to ~ -750 km s⁻¹.

Comparing the absorption velocity profiles between the leaker and the nonleaker, while both show significant absorption from highly ionized gas, the absorption extends to higher velocities for the leaker (-750 km s⁻¹) than the nonleaker (-500 km s⁻¹).

5. Discussion

5.1. Outflows Traced by UV and Optical Spectra

Outflowing gas in star-forming galaxies at $z \sim 1-3$ has been reported both from optical emission lines (e.g., Genzel et al. 2011; Newman et al. 2012; Davies et al. 2019) as well as UV absorption lines (e.g., Weiner et al. 2009; Steidel et al. 2010; Martin et al. 2012; Bordoloi et al. 2014, 2016; Jones et al. 2018). These studies have found that the outflows traced by optical emission lines typically imply a dense phase that extends out to kiloparsec scales and is driven by recent star formation activity. On the other hand, the outflows traced by UV absorption can trace a diffuse phase that extends over larger galactic scales, accumulating over longer timescales. However, quite rare in the literature are studies of outflow, at any redshift, that are traced by both UV absorption lines and optical emission lines, due to the need for high-S/N data that cover both the rest-frame UV and rest-frame optical bandpasses (e.g., James et al. 2014; Wood et al. 2015).

In the Sunburst Arc, we confidently detect outflowing gas from emission lines as well as UV absorption lines. As presented in Section 4, the blueshifted broad component in [O III] 5007 implies outflowing gas with $v_{\text{out}} = 327 \pm 2$ km s⁻¹ for the leaker and $v_{\text{out}} = 454 \pm 47$ km s⁻¹ for the nonleaker. While we detect outflowing gas from UV absorption lines in both the leaker and the nonleaker, the maximum velocity of the outflow in the leaker is considerably larger (~ 750 km s⁻¹, as measured from high-ionization absorption lines) than the maximum value measured from emission lines. The nonleaker does not show this effect; the maximum velocities traced by the UV absorption lines and broad emission components are mostly consistent within the uncertainties.

This difference in the maximum velocities traced by the emission and absorption lines in the leaker may indicate different regimes of outflow. As shown in Figure 9, the absorption lines indicate outflowing material at higher velocities than are implied by the optical emission lines. Some of this outflowing material, traced by Si IV, is likely in a phase with a similar ionization state to that traced by the [O III] emission. The lack of outflow in the emission at higher velocity may directly result from a density gradient

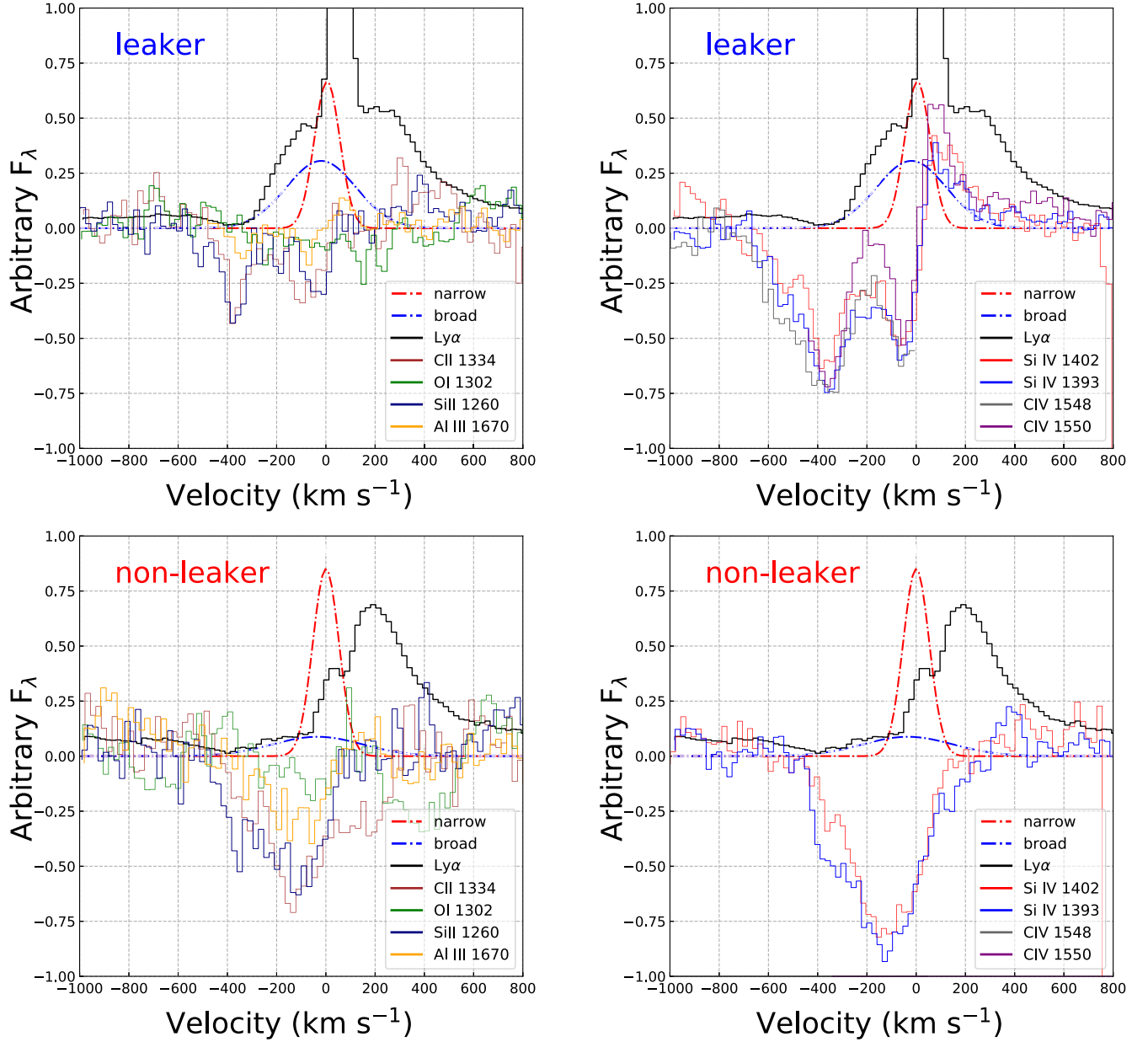


Figure 9. Comparison of the outflowing gas inferred from UV absorption lines and optical emission lines for the leaker (top panel) and the nonleaker (bottom panel). The velocity profiles from the narrow (red curve) and broad (blue curve) components of the [O III] λ 5007 emission line are plotted against low-ionization absorption lines (left panel) and high-ionization absorption lines (right panel).

(Wood et al. 2015). Indeed, in the leaker, [O II] and C III] trace very different gas densities: the electron density from [O II] (335 cm^{-3}) is similar to that of typical $z \sim 2\text{--}3$ galaxies (e.g Bian et al. 2010; Sanders et al. 2015; Steidel et al. 2016), whereas the density measured from C III] ($66,000 \text{ cm}^{-3}$) is significantly higher (Table 8).

Interestingly, the high-velocity tail of the broad emission component aligns very well with the blueshifted Ly α emission. This effect appears to be true for both the leaker and the nonleaker, although both the broad-component emission and the blueshifted Ly α emission are weaker in the nonleaker. This might indicate that the high-ionization, high-density, and high-velocity outflow regions are the same regions of low neutral gas column density that enable the Ly α (and LyC) photons to escape (Gazagnes et al. 2020).

Table 8
Electron Density Measurements for the Leaker and the Nonleaker Using [O II] and C III] Doublets

Diagnostic	Leaker (cm^{-3})	Nonleaker (cm^{-3})
C III] $\lambda\lambda$ 1907,1909	66000^{+5000}_{-3000}	19000^{+7000}_{-4000}
[O II] $\lambda\lambda$ 3727, 3729	335^{+20}_{-21}	340^{+1040}_{-340}

5.2. Why is the Leaker Leaking?

LyC escape requires both the production and leakage of UV photons. LyC production is likely associated with the most vigorously star-forming region in a galaxy (Ma et al. 2020). In the Sunburst Arc, the leaker is responsible for $18 \pm 4\%$ of the rest-frame 1500 \AA flux, which can serve as a proxy for the star formation rate (Kennicutt 1998). As such, the leaker is the most

vigorous site of star formation within its parent galaxy and is also the dominant producer of UV photons.

As shown in Figure 4, the production of UV photons is particularly high in the leaking region, which shows the spectral hallmarks of very massive stars (P-Cygni features in N V and C IV), the kind that are most effective at generating ionizing photons. A young stellar population with stellar ages of only a few million years is the primary production of LyC photons in a galaxy. Previous studies have shown that the majority of LyC photons are produced by a 1–3 Myr stellar population, with some contribution from 3–10 Myr stars (Ma et al. 2015, 2020; Kimm et al. 2017; Kim et al. 2019; Kakiichi & Gronke 2021). We have shown that the portion of the Sunburst Arc that is emitting LyC is considerably younger than the rest of the galaxy, with light-weighted ages of 3.3 versus 11.8 Myr. Thus, we attribute the youth of the leaker’s stellar population to its prodigious production of ionizing photons. By contrast, the older stellar population of the rest of the galaxy is unable to produce ionizing photons.

Thus, the generation of LyC photons has a clear physical cause: young stars. By contrast, the physical processes responsible for the escape of those photons are not well established. Two mechanisms have been proposed in the literature. The first mechanism is mechanical feedback, in the form of SNe activity or stellar winds (which occur at younger timescales than SNe), which would clear out neutral gas surrounding the young stellar cluster, such that LyC photons could eventually escape (e.g., Wise & Cen 2009; Heckman et al. 2011; Sharma et al. 2017; Hogarth et al. 2020). The second mechanism is the ionization of the surrounding gas from young stellar populations, thus creating a density-bounded H II region in which LyC photons penetrate through the low-column density region (Jaskot & Oey 2013; Nakajima & Ouchi 2014). Both processes may act together to facilitate LyC escape.

The rest-frame UV spectra (Figure 9) imply that the LyC photons are escaping because there is a deficit of low-ionization gas, which is present in abundance only ~ 400 pc away. The presence of some neutral gas along the line of sight is evident from the weak low-ionization absorption gas. This supports there being some neutral gas along the line of sight, with models of the Ly α line favoring a model with narrow ionized channels, as per that of Rivera-Thorsen et al. (2017).

5.3. Physical Scale of Ionized Outflow

A key open question in modern astrophysics is how the “feedback” from young star clusters is able to regulate star formation over the spatial scales of a whole galaxy. Fortunately, gravitational magnification allows the spatially resolved study of these processes in the Sunburst Arc, where a single star-forming region dominates the ionizing photon production and escapes at a spatial resolution that is difficult to achieve in the local universe, and impossible without lensing in the distant universe.

The leaking region shows clear evidence of ionized outflowing gas (Figure 7), which is considerably weaker in the nonleaking portions of the galaxy. Such a strong gas outflow is likely driven by recent star formation activity in the LyC leaking region. It is unclear whether the weak broad component seen in the nonleaker arises in the nonleaking region, or whether it is just an extension of the leaker’s outflow that reaches to the nonleaking regions. Whichever the case, it is

clear that the strongly ionized outflows are spatially associated with the leaker. The high-ionization absorption lines further support this—they are much stronger in the leaker compared to the nonleaking regions (Figure 9).

Further examination of the individual nonleaking regions allows us to constrain the spatial extent of the outflow. Three different FIRE pointings targeting nonleaking regions probe physical regions in the source plane that are at different distances from the leaker (Sharon et al. 2022). It is clear from Figure 8 that the outflows probed by the [O III]5007 emissions are strongest in the LyC region. At the distances of 400–700 pc that the nonleaking FIRE pointings probe, the intrinsic line flux in the outflow reduces by $>80\%$. Thus, we constrain the physical scale of the ionized outflow to <400 pc.

5.4. Evidence of an Ionized Superbubble in the Sunburst Arc?

A detailed picture of the physics of LyC escape requires probing the ISM structure and feedback from young stars on subkiloparsec spatial resolution scales. This has been challenging to achieve, both theoretically and observationally. Most recently, Ma et al. (2020) studied LyC escape from 34 $z > 5$ galaxies in high-resolution cosmological simulations. They found that the majority of the LyC escape came from very young (<10 Myr), vigorously star-forming regions of the galaxy. These regions may reside in a kiloparsec-scale ionized bubble, presumably created by SNe activity from 3–10 Myr stars. Low-column density sightlines can be fully ionized by young stars, allowing the escape of ionizing photons. In contrast, the galaxy may contain several other nonleaking regions dominated by young stars, but still embedded in dense neutral clouds. Feedback from young stars in the nonleaking regions is not strong enough to clear pathways for LyC escape.

The LyC emitting region in the Sunburst Arc is the most vigorous star-forming region in the galaxy and includes the youngest stars (~ 3 Myr) in the galaxy. The stellar feedback from such a young stellar population is likely driving the ionized outflowing gas. Over time (3–10 Myr), such ionized outflowing gas may become a giant ionized superbubble surrounding the star formation site. In such a scenario, the strongly localized outflows seen in the emission lines of the leaker may indicate that the LyC region lies within a superbubble.

Recently, Menacho et al. (2019) reported evidence of a kiloparsec-scale superbubble in a local LyC emitter (Haro 11), which may have cleared channels for LyC escape in the galaxy. This seems quite analogous to the <400 pc bubble of ionized gas in the Sunburst Arc. Superbubbles may be important mechanisms for enabling LyC photons to escape galaxies. An upcoming IFU study with JWST (GO: 2555; PI: T Rivera-Thorsen) will measure the physical size of the superbubble in the Sunburst Arc, and obtain a detailed picture of the gas kinematics in this remarkable ionizing lensed galaxy.

6. Summary and Conclusions

In this paper, we present a spectroscopic study of multiple star-forming regions within the LyC emitting galaxy, the Sunburst Arc, at $z = 2.37$. We obtain near-IR spectra from Magellan/FIRE and optical spectra from Magellan/MagE. One of the primary goals of the paper is to understand the physical conditions that facilitate the production and escape of LyC photons from a galaxy. In order to achieve our goal, we

generate rest-frame UV and rest-frame optical stacked spectra for two regions: those that emit ionizing photons (the leaker stack) and those that do not emit ionizing photons (the nonleaker stack).

The rest-frame optical spectra reveal highly ionized gas flowing out of the Sunburst Arc. The leaker shows blueshifted broad-component optical emission ($\text{FWHM} = 327 \pm 2 \text{ km s}^{-1}$) in addition to a narrow component ($\text{FWHM} = 112 \pm 1 \text{ km s}^{-1}$), which indicates the presence of strongly ionized outflowing gas. This outflow is strongest in the spectra of the leaker. Indeed, most ($54.5\% \pm 0.3\%$) of the [O III] 5007 emissions from the leaker emerge from a broad component. The stacked nonleaker spectra also show this broad component, but it accounts for only $26.1\% \pm 7.0\%$ of the [O III] 5007 emissions. Examining the spectra of the individual nonleaking components (Figure 8), the broad component decreases with increasing distance from the leaker.

The high-ionization gas traced by rest-frame UV absorption lines echoes the above picture: both the leaker and the nonleaker show blueshifted gas. In the nonleaker, this gas is centered at -200 km s^{-1} and extends to 600 km s^{-1} ; in the leaker, the absorption has two peaks, at -50 km s^{-1} and -350 km s^{-1} , and extends all the way to -750 km s^{-1} . Thus, the spectra of both the leaking and nonleaking regions show evidence for a high-velocity, high-ionization outflow, which extends to higher velocities in the leaker. The rest-frame UV absorption lines provide something that the rest-frame optical emission lines do not: a picture of the low-ionization gas, as traced by Si II 1260, CII 1334, and Al III 1670. The nonleaker shows absorption centered at -200 km s^{-1} , extending from 0 to -500 km s^{-1} . In the leaker, this low-ionization gas is much weaker, with two very weak absorption features at $\sim -50 \text{ km s}^{-1}$ – $\sim -375 \text{ km s}^{-1}$.

The rest-frame UV stacked spectra show features that are characteristic of massive stars (Figure 4). In particular, the leaker shows strong P-Cygni N V and C IV features, as well as broad He II emission; all are characteristic of young massive stars. In contrast, these features are weaker in the nonleaker stack. The stellar population fitting to the rest-frame UV spectra reveals that the leaker is considerably younger ($\sim 3 \text{ Myr}$) than the nonleaker ($\sim 12 \text{ Myr}$).













Thus, we see a consistent picture, in which the only region of the Sunburst Arc that is known to be leaking ionizing photons—the “leaker”—is also the only region showing spectral signatures of the young massive stars that are capable of producing large numbers of ionizing photons. The sightlines to the leaker appear to have little neutral gas along the line of sight, as indicated by the weak low-ionization absorption lines. What gas is present appears to be highly ionized, as is evident in the high-ionization absorption lines. The broad component of the [O III] emission suggests that stellar feedback is what has cleared out these channels. This picture supports a model for LyC escape in which the LyC photons stream out of channels cleared through the ISM.

By contrast, the nonleaking regions lack the signposts of a very young stellar population, have stronger low-ionization absorption features, which suggest substantial neutral gas along the line of sight, and have a much weaker broad velocity component of [O III]. In other words, in the nonleaking regions, we see no evidence that ionizing photons are being created, we do not see clear paths via which ionizing photons could escape, nor do we see evidence of stellar feedback that could clear out

these paths. The Sunburst Arc may be one of the best places to catch these feedback processes in action.

We thank the referee for the useful comments. The author is grateful to Daniel Stark for enlightening conversation. This material is based upon work supported by NASA, under award number 80GSFC21M0002. Based on observations made with the NASA/ESA Hubble Space Telescope, obtained at the Space Telescope Science Institute, which is operated by the Association of Universities for Research in Astronomy, Inc., under NASA contract NAS 5-26555. These observations are associated with program GO-15101. Support for Program number GO-15101 was provided through a grant from the STScI, under NASA contract NAS5-26555. Support for this work was provided by the National Aeronautics and Space Administration through Chandra Award Number GO8-19084X, issued by the Chandra X-ray Center, which is operated by the Smithsonian Astrophysical Observatory for and on behalf of the National Aeronautics Space Administration, under contract NAS8-03060. The scientific results reported in this article are based on observations made by the Chandra X-ray Observatory, and this research has made use of software provided by the Chandra X-ray Center (CXC) in the application package CIAO. This paper includes data gathered with the 6.5 m Magellan Telescopes located at Las Campanas Observatory, Chile. We thank the staff of Las Campanas for their dedicated service, which made these observations possible. We thank the telescope allocation committees of the Carnegie Observatories, The University of Chicago, The University of Michigan, and Harvard University for supporting this observing program over several years.

ORCID iDs

Ramesh Mainali  <https://orcid.org/0000-0003-0094-6827>
 Jane R. Rigby  <https://orcid.org/0000-0002-7627-6551>
 John Chisholm  <https://orcid.org/0000-0002-0302-2577>
 Matthew Bayliss  <https://orcid.org/0000-0003-1074-4807>
 Rongmon Bordoloi  <https://orcid.org/0000-0002-3120-7173>
 Michael D. Gladders  <https://orcid.org/0000-0003-1370-5010>
 T. Emil Rivera-Thorsen  <https://orcid.org/0000-0002-9204-3256>
 Håkon Dahle  <https://orcid.org/0000-0003-2200-5606>
 Keren Sharon  <https://orcid.org/0000-0002-7559-0864>
 Michael Florian  <https://orcid.org/0000-0001-5097-6555>
 Danielle A. Berg  <https://orcid.org/0000-0002-4153-053X>
 M. Riley Owens  <https://orcid.org/0000-0002-2862-307X>
 Keunho J. Kim  <https://orcid.org/0000-0001-6505-0293>

References

- Alexandroff, R. M., Heckman, T. M., Borthakur, S., Overzier, R., & Leitherer, C. 2015, *ApJ*, **810**, 104
 Amorín, R., Fontana, A., Pérez-Montero, E., et al. 2017, *NatAs*, **1**, 0052
 Baldwin, J. A., Phillips, M. M., & Terlevich, R. 1981, *PASP*, **93**, 5
 Berg, D. A., Chisholm, J., Erb, D. K., et al. 2021, *ApJ*, **922**, 170
 Berg, D. A., Erb, D. K., Auger, M. W., Pettini, M., & Brammer, G. B. 2018, *ApJ*, **859**, 164
 Berg, D. A., Skillman, E. D., Henry, R. B. C., Erb, D. K., & Carigi, L. 2016, *ApJ*, **827**, 126
 Bian, F., Fan, X., Bechtold, J., et al. 2010, *ApJ*, **725**, 1877
 Bian, F., Fan, X., McGreer, I., Cai, Z., & Jiang, L. 2017, *ApJL*, **837**, L12
 Bordoloi, R., Lilly, S. J., Hardmeier, E., et al. 2014, *ApJ*, **794**, 130
 Bordoloi, R., Rigby, J. R., Tumlinson, J., et al. 2016, *MNRAS*, **458**, 1891

- Borthakur, S., Heckman, T. M., Leitherer, C., & Overzier, R. A. 2014, *Sci*, **346**, 216
- Brammer, G. 2018, Gbrammer/Grizli: Preliminary Release, v0.4.0, Zenodo, doi:10.5281/zenodo.1146905
- Cardelli, J. A., Clayton, G. C., & Mathis, J. S. 1989, *ApJ*, **345**, 245
- Chisholm, J., Orlitová, I., Schaerer, D., et al. 2017, *A&A*, **605**, A67
- Chisholm, J., Rigby, J. R., Bayliss, M., et al. 2019, *ApJ*, **882**, 182
- Dahle, H., Aghanim, N., Guennou, L., et al. 2016, *A&A*, **590**, L4
- Davies, R. L., Förster Schreiber, N. M., Übler, H., et al. 2019, *ApJ*, **873**, 122
- Du, X., Shapley, A. E., Reddy, N. A., et al. 2018, *ApJ*, **860**, 75
- Finkelstein, S. L., D'Aloisio, A., Paardekooper, J.-P., et al. 2019, *ApJ*, **879**, 36
- Fletcher, T. J., Tang, M., Robertson, B. E., et al. 2019, *ApJ*, **878**, 87
- Florian, M. K., Rigby, J. R., Acharyya, A., et al. 2021, *ApJ*, **916**, 50
- Flury, S. R., Jaskot, A. E., Ferguson, H. C., et al. 2022a, *ApJS*, **260**, 1
- Flury, S. R., Jaskot, A. E., Ferguson, H. C., et al. 2022b, *ApJ*, **930**, 126
- Gazagnes, S., Chisholm, J., Schaerer, D., Verhamme, A., & Izotov, Y. 2020, *A&A*, **639**, A85
- Genzel, R., Newman, S., Jones, T., et al. 2011, *ApJ*, **733**, 101
- Gnedin, N. Y., Kravtsov, A. V., & Chen, H.-W. 2008, *ApJ*, **672**, 765
- Green, G. M., Schlafly, E. F., Finkbeiner, D. P., et al. 2015, *ApJ*, **810**, 25
- Heckman, T. M., Borthakur, S., Overzier, R., et al. 2011, *ApJ*, **730**, 5
- Hogarth, L., Amorín, R., Vílchez, J. M., et al. 2020, *MNRAS*, **494**, 3541
- Hopkins, P. F., Wetzell, A., Kereš, D., et al. 2018, *MNRAS*, **480**, 800
- Izotov, Y. I., Schaerer, D., Thuan, T. X., et al. 2016, *MNRAS*, **461**, 3683
- Izotov, Y. I., & Thuan, T. X. 2008, *ApJ*, **687**, 133
- Izotov, Y. I., Worseck, G., Schaerer, D., et al. 2018, *MNRAS*, **478**, 4851
- Izotov, Y. I., Worseck, G., Schaerer, D., et al. 2021, *MNRAS*, **503**, 1734
- James, B. L., Pettini, M., Christensen, L., et al. 2014, *MNRAS*, **440**, 1794
- Jaskot, A. E., & Oey, M. S. 2013, *ApJ*, **766**, 91
- Jones, T., Ellis, R. S., Richard, J., & Jullo, E. 2013, *ApJ*, **765**, 48
- Jones, T., Stark, D. P., & Ellis, R. S. 2018, *ApJ*, **863**, 191
- Kakiichi, K., & Gronke, M. 2021, *ApJ*, **908**, 30
- Kauffmann, G., Heckman, T. M., Tremonti, C., et al. 2003, *MNRAS*, **346**, 1055
- Kelson, D. D. 2003, *PASP*, **115**, 688
- Kennicutt, R. C. J. 1998, *ARA&A*, **36**, 189
- Kim, J.-G., Kim, W.-T., & Ostriker, E. C. 2019, *ApJ*, **883**, 102
- Kim, J.-h., Krumholz, M. R., Wise, J. H., et al. 2013, *ApJ*, **775**, 109
- Kim, K., Malhotra, S., Rhoads, J. E., Butler, N. R., & Yang, H. 2020, *ApJ*, **893**, 134
- Kimm, T., Katz, H., Haehnelt, M., et al. 2017, *MNRAS*, **466**, 4826
- Kroupa, P. 2001, *MNRAS*, **322**, 231
- Kulkarni, G., Worseck, G., & Hennawi, J. F. 2019, *MNRAS*, **488**, 1035
- Labbé, I., Oesch, P. A., Bouwens, R. J., et al. 2013, *ApJL*, **777**, L19
- Leitet, E., Bergvall, N., Hayes, M., Linné, S., & Zackrisson, E. 2013, *A&A*, **553**, A106
- Leitet, E., Bergvall, N., Piskunov, N., & Andersson, B. G. 2011, *A&A*, **532**, A107
- Leitherer, C., Ekström, S., Meynet, G., et al. 2014, *ApJS*, **212**, 14
- Leitherer, C., Hernandez, S., Lee, J. C., & Oey, M. S. 2016, *ApJ*, **823**, 64
- Leitherer, C., Ortiz Otálvaro, P. A., Bresolin, F., et al. 2010, *ApJS*, **189**, 309
- Leitherer, C., Schaerer, D., Goldader, J. D., et al. 1999, *ApJS*, **123**, 3
- Ma, X., Kasen, D., Hopkins, P. F., et al. 2015, *MNRAS*, **453**, 960
- Ma, X., Quataert, E., Wetzell, A., et al. 2020, *MNRAS*, **498**, 2001
- Madau, P., & Haardt, F. 2015, *ApJL*, **813**, L8
- Mainali, R., Stark, D. P., Tang, M., et al. 2020, *MNRAS*, **494**, 719
- Marshall, J. L., Burles, S., Thompson, I. B., et al. 2008, *Proc. SPIE*, **7014**, 701454
- Martin, C. L., Shapley, A. E., Coil, A. L., et al. 2012, *ApJ*, **760**, 127
- Menacho, V., Östlin, G., Bik, A., et al. 2019, *MNRAS*, **487**, 3183
- Naidu, R. P., Matthee, J., Oesch, P. A., et al. 2022, *MNRAS*, **510**, 4582
- Nakajima, K., & Ouchi, M. 2014, *MNRAS*, **442**, 900
- Newman, S. F., Genzel, R., Förster-Schreiber, N. M., et al. 2012, *ApJ*, **761**, 43
- Peng, C. Y., Ho, L. C., Impey, C. D., & Rix, H.-W. 2010, *AJ*, **139**, 2097
- Reddy, N. A., Steidel, C. C., Pettini, M., & Bogosavljević, M. 2016, *ApJ*, **828**, 107
- Rigby, J. R., Bayliss, M. B., Chisholm, J., et al. 2018, *ApJ*, **853**, 87
- Rigby, J. R., Florian, M., Acharyya, A., et al. 2021, *ApJ*, **908**, 154
- Rivera-Thorsen, T. E., Dahle, H., Chisholm, J., et al. 2019, *Sci*, **366**, 738
- Rivera-Thorsen, T. E., Dahle, H., Gronke, M., et al. 2017, *A&A*, **608**, L4
- Robertson, B. E., Ellis, R. S., Furlanetto, S. R., & Dunlop, J. S. 2015, *ApJL*, **802**, L19
- Rosdahl, J., Katz, H., Blaizot, J., et al. 2018, *MNRAS*, **479**, 994
- Rubin, K. H. R., Prochaska, J. X., Koo, D. C., et al. 2014, *ApJ*, **794**, 156
- Sanders, R. L., Shapley, A. E., Kriek, M., et al. 2015, *ApJ*, **799**, 138
- Sanders, R. L., Shapley, A. E., Kriek, M., et al. 2016, *ApJ*, **816**, 23
- Schaerer, D., Izotov, Y. I., Worseck, G., et al. 2022, *A&A*, **658**, L11
- Shapley, A. E., Steidel, C. C., Strom, A. L., et al. 2016, *ApJL*, **826**, L24
- Sharma, M., Theuns, T., Frenk, C., et al. 2017, *MNRAS*, **468**, 2176
- Sharon, K., Gladders, M. D., Rigby, J. R., et al. 2012, *ApJ*, **746**, 161
- Sharon, K., Mahler, G., Rivera-Thorsen, T. E., et al. 2022, arXiv:2209.03417
- Simcoe, R. A., Burgasser, A. J., Bernstein, R. A., et al. 2008, *Proc. SPIE*, **7014**, 70140U
- Stark, D. P., Auger, M., Belokurov, V., et al. 2013, *MNRAS*, **436**, 1040
- Steidel, C. C., Bogosavljević, M., Shapley, A. E., et al. 2018, *ApJ*, **869**, 123
- Steidel, C. C., Erb, D. K., Shapley, A. E., et al. 2010, *ApJ*, **717**, 289
- Steidel, C. C., Strom, A. L., Pettini, M., et al. 2016, *ApJ*, **826**, 159
- Storey, P. J., & Zeippen, C. J. 2000, *MNRAS*, **312**, 813
- Vanzella, E., Castellano, M., Meneghetti, M., et al. 2017, *ApJ*, **842**, 47
- Vanzella, E., De Barros, S., Cupani, G., et al. 2016, *ApJL*, **821**, L27
- Vanzella, E., Meneghetti, M., Pastorello, A., et al. 2020, *MNRAS*, **499**, L67
- Vanzella, E., Nonino, M., Cupani, G., et al. 2018, *MNRAS*, **476**, L15
- Weiner, B. J., Coil, A. L., Prochaska, J. X., et al. 2009, *ApJ*, **692**, 187
- Wise, J. H., & Cen, R. 2009, *ApJ*, **693**, 984
- Wise, J. H., Demchenko, V. G., Halicek, M. T., et al. 2014, *MNRAS*, **442**, 2560
- Wood, C. M., Tremonti, C. A., Calzetti, D., et al. 2015, *MNRAS*, **452**, 2712